

Monitoring Vibrational Evolution in Jahn-Teller Effect by Raman Images

Hai-Zhen Yu,¹ Dingwei Chu,¹ Yuanzhi Li,¹ Li Wang,¹ Yuzhi Song,¹ Sai Duan,^{2,3,*} Chuan-Kui Wang,^{1,†} and Zhen Xie^{1,‡}

¹*Shandong Province Key Laboratory of Medical Physics and Image Processing Technology, School of Physics and Electronics, Shandong Normal University, Jinan 250014, P.R. China.*

²*Collaborative Innovation Center of Chemistry for Energy Materials, Shanghai Key Laboratory of Molecular Catalysis and Innovative Materials, MOE Key Laboratory of Computational Physical Sciences, Department of Chemistry, Fudan University, Shanghai 200433, P.R. China*

³*Hefei National Laboratory, Hefei 230088, P.R. China*

(Dated: February 17, 2025)

The Jahn-Teller effect (JTE) reduces the geometrical symmetry of a system with degenerate electronic states via vibronic coupling, playing a pivotal role in molecular and condensed systems. In this Letter, we propose that vibrational resolved tip-enhanced Raman scattering images can visualize the vibrational evolutions in JTE in real space. Taking an experimentally viable single zinc phthalocyanine (ZnPc) molecule as a proof-of-principle example, not only the degenerate vibrational splitting but also the overlooked vibration mixing caused by the JTE in its anionic form can be straightforwardly characterized by Raman images. Leveraging Raman images, the controllable configuration of JTE distortion with partial isotopic substitution could be further identified. These findings establish a practical protocol to monitor the detailed vibrational evolutions when a single molecule experiences JTE, opening a door for visualization of spontaneous symmetry breaking in molecular and solid-state systems.

The Jahn-Teller effect (JTE)[1, 2] describes a fundamental phenomenon that a degenerate system spontaneously reduces its geometry symmetry via the vibronic coupling to stabilize the total energy[3–5]. JTE represents a general mechanism of spontaneous symmetry breaking, which is responsible for various important observations across multiple disciplines, including spectroscopy, molecular and solid-state physics, stereochemistry, and materials science[6–12]. In practice, JTE can be efficiently induced by injecting or removing an electron from a degenerate electronic state[13–15], particularly in systems containing transition metal ions[7, 16, 17]. In this context, scanning probe microscopy (SPM) techniques provide a unique means to precisely control JTE in real space[18, 19].

Despite the success of SPM techniques in the visualization of JTE, most investigations were focused on imaging the symmetry breaking of electronic states[20–24]. Exclusive investigation on the electronic degrees of freedom in JTE has led to a severe lack of understanding of its vibrational aspect, which results in potentially questionable assignments of accompanying frequency splitting, the overlooked mixing of vibrational wavefunctions upon symmetry reduction, and the unexplored possibility of controlling JTE distortions through atomic displacements.

Indeed, only few experiments studied the vibrational feature of JTE by SPM. For instance, by leveraging the tip-enhanced Raman scattering (TERS)[25–28], recent measurements have captured the spectral variations associated with JTE in a negatively charged zinc phthalocyanine (ZnPc⁻)[14], where frequency evolution was highlighted. To date, there have been no reports on imaging vibrational symmetry breaking, another essential aspect of JTE, although it is possible owing to the high spatial resolution of TERS[29–33].

In this Letter, taking the experimentally feasible ZnPc molecule as a proof-of-principle example, we theoretically propose that TERS images provide a powerful means to monitor all the details of the vibrational evolution in JTE distortion. We demonstrate that, not only the splitting of degenerate vibrations but also the mixing of non-degenerate vibrations belonging to different irreducible representations of the high-symmetry point group, can be affirmatively observed in TERS images. For the latter case, we reveal that the mixing strength is determined by both the energy difference and spatial distribution overlap between the mixed modes. Moreover, we manifest that the controllable JTE distortions at the sub-angstrom level achieved through partial isotope substitution can be unambiguously distinguished by high-resolution TERS imaging.

Figure 1(a) illustrates the experimental setup for injecting an electron into neutral ZnPc to induce JTE distortion. Previous experiments observed sudden changes in TERS spectra when the sample bias exceeded 0.3 V, which was assigned as a transition from the neutral to negatively charged state[14]. It should be stressed that owing to the insulating spacer layer introduced in

* duansai@fudan.edu.cn

† ckwang@sdsu.edu.cn

‡ xiezhen@sdsu.edu.cn

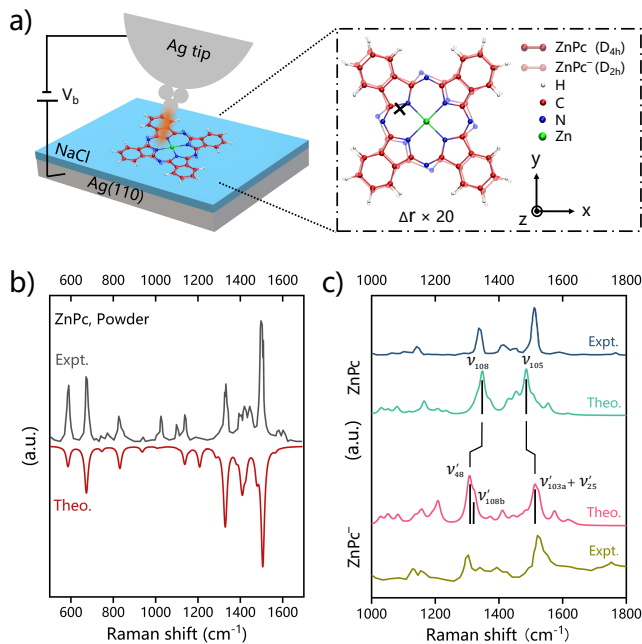


FIG. 1. (a) Schematic of experimental TERS measurement for charge-induced JTE in a ZnPc molecule. The relative geometrical differences between ZnPc and ZnPc $^-$ were amplified by a factor of 20 for a better illustration. The black cross mark indicated the plasmon central position for the TERS spectra in (c). (b) Experimental (gray line) and theoretical (red line) normal Raman spectra of ZnPc powder. (c) Experimental and theoretical (under a 3 Å plasmon) TERS spectra of ZnPc and ZnPc $^-$ with plasmon center focused on the black marked position in (a). All the experimental spectra were extracted from Ref. 14. The label of vibrations was in accordance with Herzberg’s nomenclature[34] and the superscript “ ν ” represents the evolutionary counterparts of the anionic form.

Fig. 1(a), the negatively charged ZnPc $^-$ has a sufficiently long lifetime for spectral measurements and even imaging[14]. Besides, the JTE-induced geometrical distortion from the neutral D_{4h} to the anionic D_{2h} is quite subtle (the elongations along both the diagonal axes are 0.026 and 0.010 Å, respectively, as shown in Fig. 1(a)), which provides an ideal example for focusing exclusively on vibrational variation itself.

To efficiently excite the required highly localized plasmonic field, an incident light with a wavelength of 532 nm was employed in experiments[14]. Under the same incident energy, our first-principles calculations accurately reproduce the observed Raman spectra of ZnPc powder under the experimental conditions (Fig. 1(b))[14]. Furthermore, by placing a 3 Å localized plasmon in the same position in experiments, i.e., above the lobe of ZnPc (see the black cross in Fig. 1(a)), the calculated TERS spectra for both neutral ZnPc and anionic ZnPc $^-$ obtained using the effective field Hamiltonian[31, 35–38] (also see Section S1 in Supplemental Material) agree well with their experimental counterparts (Fig. 1(c)).

Specifically, the calculated TERS spectrum of ZnPc $^-$ presents a 39.1 cm^{-1} redshift and 25.8 cm^{-1} blueshift compared with the two dominant bands around 1348 and 1486 cm^{-1} in ZnPc, respectively, which consistently reproduces the correspondingly observed 45 cm^{-1} redshift and 22 cm^{-1} blueshift in experiments[14]. The quantitative reproduction of the measured references in both uniform and plasmonic fields validates the accurate descriptions of electronic and vibrational structures as well as their responses at the current theoretical level.

According to the calculations, the experimentally measured[14] two dominant bands for ZnPc and ZnPc $^-$ (Fig. 1(c)) are assigned to different vibrational modes. Specifically, the degenerate ν_{108} and ν_{105} contribute to the dominant bands of ZnPc. In ZnPc $^-$, these vibrations split as a consequence of JTE and are labeled with subscripts “a” and “b” hereafter. As a result, the dominant high-frequency band originates from the occasionally degenerate ν'_{103a} and ν'_{25} , where the superscript “ ν ” denotes the anionic form. Meanwhile, ν'_{48} contributes to the dominant band with low frequency, with the shoulder assigned as ν'_{108b} . Although this assignment is different from previous reports[14], the observation of only a single splitting component, i.e., ν'_{108b} in ZnPc $^-$, indicates the spatial localization of degenerate vibrational modes during symmetry breaking induced by JTE.

To directly visualize the localization, we turn to vibrationally resolved TERS imaging[39–43]. By moving tip positions and simultaneously collecting scattering intensities at a given Raman shift, the images of dominant bands of ZnPc were calculated as shown in Fig. 2(a). Both images exhibit clear four-fold symmetrical patterns, which correspond to the E_u irreducible representation in D_{4h} point group (see vibrational displacements in Fig. 2(a)). On the other hand, the dominant modes of ZnPc $^-$ give two-fold symmetric patterns (Fig. 2(a)), demonstrating the symmetry reduction from D_{4h} to D_{2h} owing to JTE. The individual contributions of component modes to images in Fig. 2(a) can be found in Figs. S1-S3 (Section S2).

Detailed analysis reveals that at the central Zn position, the image of ν'_{48} is constructive, which is opposite to the destructive feature in that of ν_{108} . This result further confirms that the dominant bands observed in experiments[14] originate from different vibrational modes. To determine the split modes of degenerate vibrations, for example, ν_{108} that involves vibrations at four interior nitrogen atoms, we focused the plasmon field on the nitrogen atoms along different axes in ZnPc $^-$ (see the color-marked crosses in the inset of Fig. 2(b)). The calculated spectra manifest that one split mode becomes active, while another one is completely suppressed (Fig. 2(b)). As a result, the split modes (ν'_{108a} and ν'_{108b}) can be identified. TERS images of these vibrations exhibit split patterns derived from the original ν_{108} , with a destructive center, as anticipated (Fig. 2(c)).

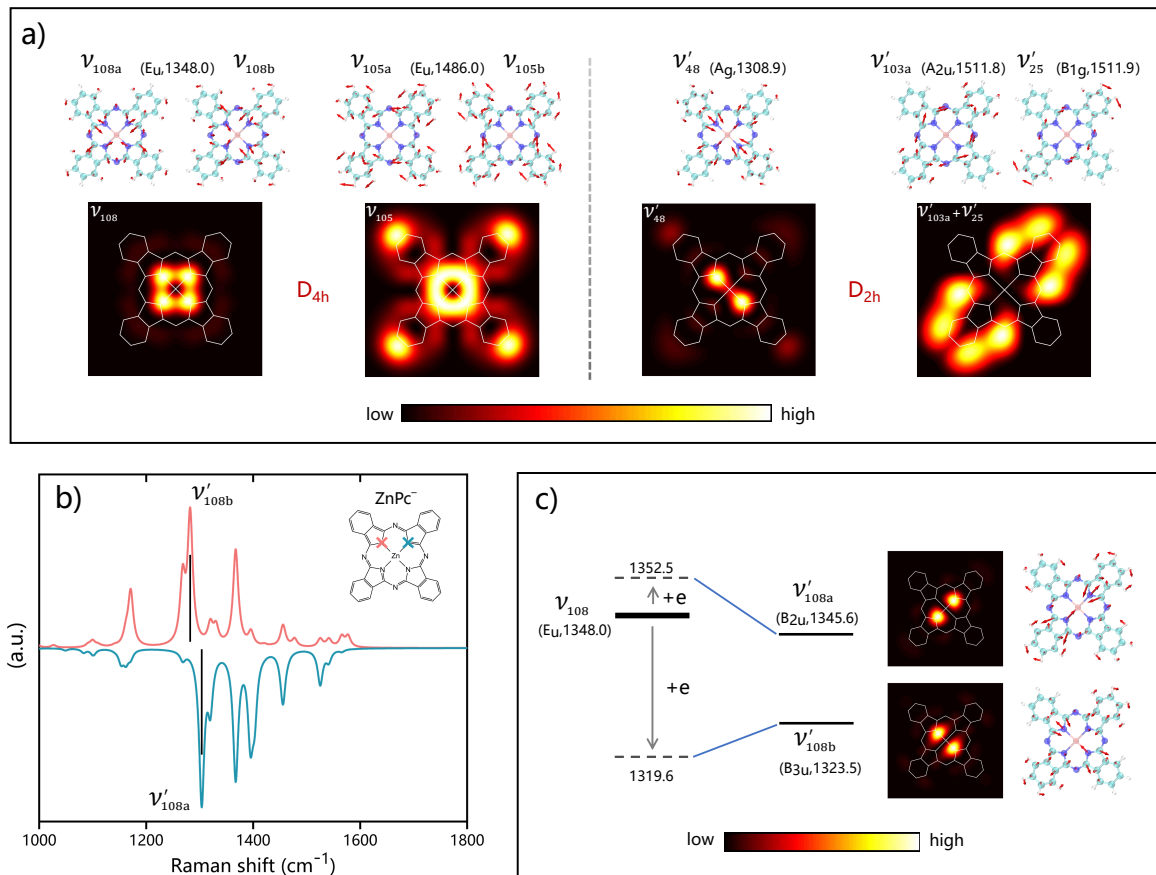


FIG. 2. (a) Calculated Raman images under a 3 Å plasmon for the dominant bands of ZnPc (left) and ZnPc⁻ (right) as shown in Fig. 1(c). The corresponding vibrational modes, frequencies, and irreducible representations were depicted for comparison. (b) Calculated TERS spectra under a 3 Å plasmon located at nitrogen atoms of different axes in ZnPc⁻ (marked by crosses). (c) Illustration of the splitting of the degenerate vibrational mode ν_{108} due to charge-induced JTE. The electronic effect of the excess electron on the vibrational energy of ν_{108} was indicated by arrows. The calculated Raman images and corresponding vibrational modes for the splitting modes in ZnPc⁻ were depicted.

With the correct assignment, the electronic and displacement redistribution effects can be unambiguously investigated for the splitting of degenerate vibrations when the molecule experiences a JTE distortion. Particularly, adding an extra electron to neutral D_{4h} ZnPc would split the degenerate ν_{108} at 1348.0 cm⁻¹ into a blue-shifted mode at 1352.5 cm⁻¹ and a significantly red-shifted mode at 1319.6 cm⁻¹. The E_u ν_{108} mode then becomes further localized, which results in two non-degenerate modes, i.e., a B_{2u} mode (ν'_{108a}) at 1345.6 cm⁻¹ and a B_{3u} mode (ν'_{108b}) at 1323.5 cm⁻¹ (Fig. 2(c)). The decomposition of electronic and vibrational effects is a general approach. The detailed analysis for other representative degenerate modes can be found in Fig. S4. It should be stressed that the minor geometrical distortion caused by JTE in ZnPc enables the decomposition of these effects.

The minor geometrical distortion also allows explicit visualization of another vibrational evolution, i.e., the

mixing of non-degenerate vibrations in high symmetry after experiencing JTE (Table S1), a phenomenon completely overlooked in previous studies. For instance, the A_{2g}-symmetric ν_{23} and B_{2g}-symmetric ν_{65} in ZnPc would mix with each other, generating two B_{1g} modes (ν'_{23} and ν'_{65}) in ZnPc⁻ (Fig. 3(a)). A detailed decomposition reveals that the electronic effect leads to redshifts of two modes, resulting in a frequency difference of 4.4 cm⁻¹. It is noted that the displacements of ν_{23} and ν_{65} are all located on the lobes with an efficient overlap. Calculated induced dipole moments (Figs. S5 and S6) determine that the mixing coefficient (see definition in Eq. 1) between ν_{23} and ν_{65} is close to 1.0, which results in distinctly split patterns in ν'_{23} and ν'_{65} as shown in Fig. 3(a).

The mixing coefficient could be analogously derived from the perturbational molecular orbital theory as (see a detailed derivation in Section S3)

$$T = \frac{\lambda S_{12}}{\Delta E - \lambda S_{12}^2}, \quad (1)$$

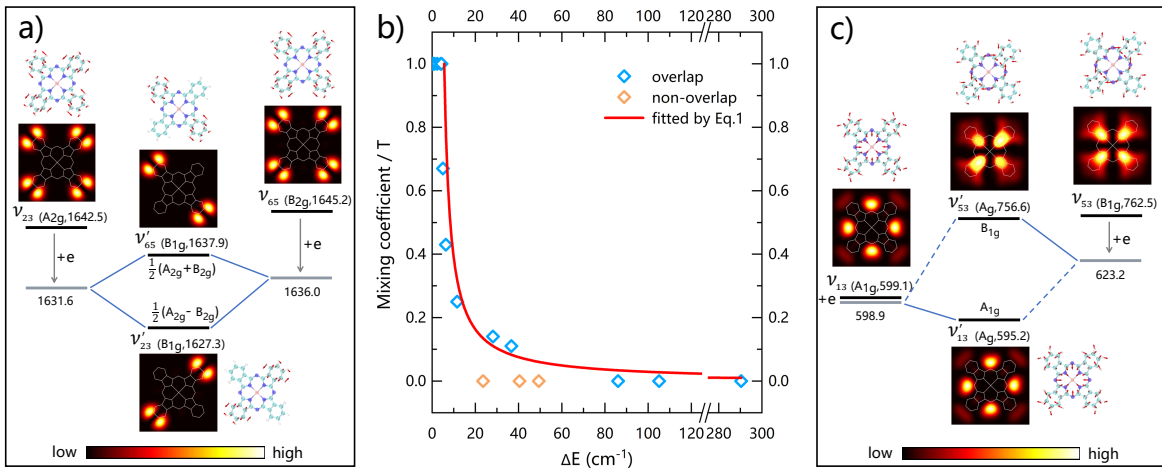


FIG. 3. Evolution of non-degenerate vibrational mixing from ZnPc to ZnPc⁻. (a) Mixing of well-overlapped ν_{23} and ν_{65} modes. (b) Relationship between the mixing coefficient T and the energy difference ΔE for mixed modes, fitted by Eq. 1 (the red line) and measured by Raman images (the diamond scatters). (c) Mixing of non-overlapped ν_{13} and ν_{53} modes.

where λ is a fitting parameter, S_{12} is the overlap between two mixing vibrations, and ΔE is the energy difference. For well-overlapped modes, i.e., S_{12} close to 1, the mixing coefficient T is inversely proportional to the energy difference ΔE , which is exactly the case of mode mixing for ν_{23} and ν_{65} . Most of the mixing modes are in this category (Figs. S7-S9). By collecting all these modes, the fitting parameter λ is determined to be 2.8 cm⁻¹ (see the blue diamond scatters and red line in Fig. 3(b)).

The theoretical model also predicts another category with $S_{12} = 0$, where T becomes zero regardless of ΔE and λ . In fact, there are few modes belonging to this category. For instance, the electronic effect leads to ΔE of 24.3 cm⁻¹ between the A_{1g}-symmetric ν_{13} and B_{1g}-symmetric ν_{53} modes. If they were well-overlapped modes, the predicted T would be 0.13. Nevertheless, with no mixing with each other, these two modes give two A_g-symmetric modes in ZnPc⁻, exhibiting nearly identical four-fold image characteristics to their respective counterparts in ZnPc (Fig. 3(c)). This result should be attributed to the lack of spatial overlap between ν_{13} and ν_{53} modes, which is the sufficient prerequisite of $S_{12} = 0$. Two additional cases fall into this category (see orange diamond scatters in Fig. 3(b) and Fig. S10).

The last capability of TERS imaging proposed in the present work is the identification of the controllable distortion in JTE. To this end, partial isotope substitution is employed to control the direction of JTE distortion. Although the geometrical variation is quite small (Fig. 1(a)), isotope substitutions of ¹³C and deuterium (D) in one diagonal axis can stabilize the ZnPc⁻'s elongation configuration along this axis, i.e., iso-1 (Fig. 4(a)). Calculated results reveal that at the experimental conditions of 7 K and 6 × 10⁻¹⁴ atm, iso-1 has a lower Gibbs free energy of 0.38 kJ/mol than the configuration elon-

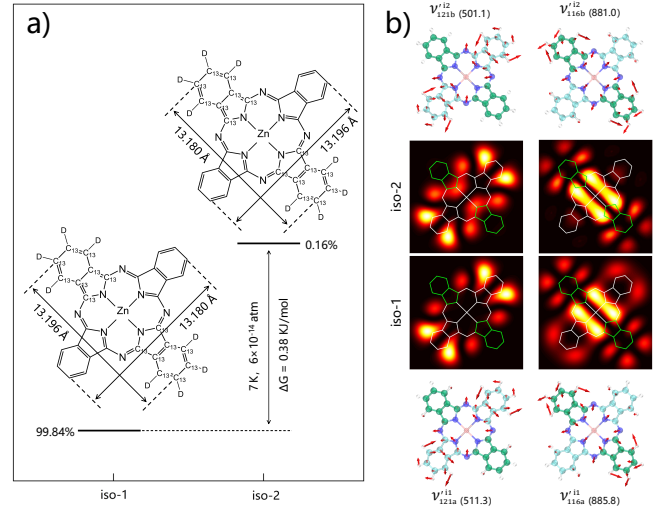


FIG. 4. Identification of JTE distortion in partially isotopic ZnPc⁻. (a) Two isomers (iso-1 and iso-2) of ZnPc⁻ with partial isotope substitutions of carbon-13 (¹³C) and deuterium (D) in one diagonal axis. The labeled values are the calculated free energy difference between the two isomers and their corresponding Boltzmann populations under conditions of 7 K and 6 × 10⁻¹⁴ atm. (b) Representative Raman images for analogical modes in iso-1 and iso-2. The isotopic axis in vibrational modes and molecular skeletons was highlighted in green.

gated along the other direction (iso-2). The population of iso-1 is then determined to be 99.84% in the experimental conditions (Section S4). Because of the almost identical geometries (Fig. 4(a)), iso-1 and iso-2 are indistinguishable in electronic structure-based SPM techniques.

Remarkably, vibrationally resolved TERS images have the ability to overcome this challenge (Fig. 4(b)). Although the calculated TERS image of ν_{121a}^{11} in iso-1 has

the identical brightest lobe patterns to that of the counterpart in iso-2, two moderate patterns appear around the interior nitrogen atoms along the isotopic axis for ν_{121b}^{i2} in iso-2. Similarly, except for the identical brightest central patterns, moderate patterns arise around the non-isotopic lobes in ν_{116a}^{i1} image for iso-1. These results should be attributed to the subtle vibrational redistributions caused by the axial length difference at the sub-ångström level. The ability of TERS imaging to distinguishing such subtle vibrational variations offers a unique means for identifying different configurations arising from isotopic JTE distortion.

In summary, taking the experimentally feasible ZnPc as an example, we demonstrate that vibrationally resolved Raman images have the capability to monitor detailed vibrational evolutions when molecules experience JTE distortions. The significance of identifying the most common degenerate vibrational splitting in JTE via Raman images has been highlighted. In addition, Raman images can further capture the mixing of different irreducible representations in high-symmetry point groups due to JTE. Moreover, we reveal that controllable JTE-induced distortion configurations, achieved through partial isotopic substitution, can also be distinguished via Raman imaging. These findings manifest that vibrationally resolved Raman imaging provides a unique and practical optical means for comprehensively monitoring vibrational evolutions in JTE, deepening our understanding and enabling the regulation of JTE.

This work was supported by the National Key R&D Program of China (2024YFA1208104), the National Natural Science Foundation of China (Nos. 22393911, 22373060, 22473028, and 12474258), the Innovation Program for Quantum Science and Technology (2021ZD0303301), Shandong Provincial Natural Science Foundation (projects ZR2021QB164 and ZR2024QA020), and the Taishan Scholar Project of Shandong Province (tsqn202211110).

-
- [1] H. A. Jahn, E. Teller, and F. G. Donnan, *Proc. R. Soc. Lond. A* **161**, 220 (1937).
- [2] I. B. Bersuker, *Chem. Rev.* **121**, 1463 (2021).
- [3] R. G. Pearson, *Proc. Natl. Acad. Sci.* **72**, 2104 (1975).
- [4] M. Angeli, E. Tosatti, and M. Fabrizio, *Phys. Rev. X* **9**, 041010 (2019).
- [5] H. C. Longuet-Higgins, U. Öpik, M. H. L. Pryce, and R. A. Sack, *Proc. R. Soc. Lond. A* **244**, 1 (1958).
- [6] Y. Liu, F. Guo, B. Yang, and S. Zhao, *Appl. Phys. Lett.* **119**, 233901 (2021).
- [7] Y. Y. Zhang, S. X. Du, and H. J. Gao, *Phys. Rev. B* **84**, 125446 (2011).
- [8] P. Barone, K. Yamauchi, and S. Picozzi, *Phys. Rev. B* **92**, 014116 (2015).
- [9] K. Geirhos, J. Langmann, L. Prodan, A. A. Tsrilin, A. Missiul, G. Eickerling, A. Jesche, V. Tsurkan, P. Lunkenheimer, W. Scherer, and I. Kézsmárki, *Phys. Rev. Lett.* **126**, 187601 (2021).
- [10] W. J. Kim, M. A. Smeaton, C. Jia, B. H. Goodge, B.-G. Cho, K. Lee, M. Osada, D. Jost, A. V. Ievlev, B. Moritz, L. F. Kourkoutis, T. P. Devereaux, and H. Y. Hwang, *Nature* **615**, 237 (2023).
- [11] H. Y. Huang, Z. Y. Chen, R. P. Wang, F. M. F. de Groot, W. B. Wu, J. Okamoto, A. Chainani, A. Singh, Z. Y. Li, J. S. Zhou, H. T. Jeng, G. Y. Guo, J.-G. Park, L. H. Tjeng, C. T. Chen, and D. J. Huang, *Nat. Commun.* **8**, 15929 (2017).
- [12] Y. Zhu, J.-T. Sun, J. Pan, J. Deng, and S. Du, *Phys. Rev. Lett.* **134**, 046403 (2025).
- [13] I. Báldea, *RSC Adv.* **6**, 93715 (2016).
- [14] B. Yang, G. Chen, A. Ghafoor, Y.-F. Zhang, X.-B. Zhang, H. Li, X.-R. Dong, R.-P. Wang, Y. Zhang, Y. Zhang, and Z.-C. Dong, *Angew. Chem. Int. Ed.* **62**, e202218799 (2023).
- [15] A. Choi, T. Kim, M.-H. Kim, S. W. Lee, Y. H. Jung, and H.-W. Lee, *Adv. Func. Mater.* **32**, 2111901 (2022).
- [16] J. Zhang, J.-B. Kim, J. Zhang, G.-H. Lee, M. Chen, V. W.-h. Lau, K. Zhang, S. Lee, C.-L. Chen, T.-Y. Jeon, Y.-W. Kwon, and Y.-M. Kang, *J. Am. Chem. Soc.* **144**, 7929 (2022).
- [17] F. K. Kirschner, R. D. Johnson, F. Lang, D. D. Khalyavin, P. Manuel, T. Lancaster, D. Prabhakaran, and S. J. Blundell, *Phys. Rev. B* **99**, 064403 (2019).
- [18] L. L. Patera, F. Queck, P. Scheuerer, and J. Repp, *Nature* **566**, 245 (2019).
- [19] L. L. Patera, F. Queck, P. Scheuerer, N. Moll, and J. Repp, *Phys. Rev. Lett.* **123**, 016001 (2019).
- [20] A. Wachowiak, R. Yamachika, K. H. Khoo, Y. Wang, M. Grobis, D.-H. Lee, S. G. Louie, and M. F. Crommie, *Science* **310**, 468 (2005).
- [21] I. D. Hands, J. L. Dunn, and C. A. Bates, *Phys. Rev. B* **82**, 155425 (2010).
- [22] T. Hitosugi, S. Heike, T. Onogi, T. Hashizume, S. Watanabe, Z.-Q. Li, K. Ohno, Y. Kawazoe, T. Hasegawa, and K. Kitazawa, *Phys. Rev. Lett.* **82**, 4034 (1999).
- [23] J. Kügel, P.-J. Hsu, M. Böhme, K. Schneider, J. Senkpiel, D. Serrate, M. Bode, and N. Lorente, *Phys. Rev. Lett.* **121**, 226402 (2018).
- [24] C. Li, M.-L. Bocquet, Y. Lu, N. Lorente, M. Gruber, R. Berndt, and A. Weismann, *Phys. Rev. Lett.* **133**, 126201 (2024).
- [25] R. M. Stöckle, Y. D. Suh, V. Deckert, and R. Zenobi, *Chem. Phys. Lett.* **318**, 131 (2000).
- [26] M. S. Anderson, *App. Phys. Lett.* **76**, 3130 (2000).
- [27] N. Hayazawa, Y. Inouye, Z. Sekkat, and S. Kawata, *Opt. Commun.* **183**, 333 (2000).
- [28] B. Pettinger, G. Picardi, R. Schuster, and G. Ertl, *Electrochem. Jpn.* **68**, 942 (2000).
- [29] R. Zhang, Y. Zhang, Z. Dong, S. Jiang, C. Zhang, L. Chen, L. Zhang, Y. Liao, J. Aizpurua, Y. Luo, J. Yang, and J. Hou, *Nature* **498**, 82 (2013).
- [30] J. Xu, X. Zhu, S. Tan, Y. Zhang, B. Li, Y. Tian, H. Shan, X. Cui, A. Zhao, Z. Dong, J. Yang, Y. Luo, B. Wang, and J. G. Hou, *Science* **371**, 818 (2021).
- [31] S. Duan, G. Tian, and Y. Luo, *Chem. Soc. Rev.* **53**, 5083 (2024).
- [32] S. Fang, S. Duan, X. Wang, S. Chen, L. Li, H. Li, B. Jiang, C. Liu, N. Wang, L. Zhang, X. Wen, Y. Yao, J. Zhang, D. Xie, Y. Luo, and W. Xu, *Nat. Photon.* **17**, 531 (2023).

- [33] C.-Y. Li, S. Duan, B.-Y. Wen, S.-B. Li, M. Kathiresan, L.-Q. Xie, S. Chen, J. R. Anema, B.-W. Mao, Y. Luo, *et al.*, *Nature Nanotechnol.* **15**, 922 (2020).
- [34] G. Herzberg, *Molecular spectra and molecular structure. Vol.2: Infrared and Raman spectra of polyatomic molecules* (D. Van Nostrand, Princeton, 1945).
- [35] S. Duan, G. Tian, Y. Ji, J. Shao, Z. Dong, and Y. Luo, *J. Am. Chem. Soc.* **137**, 9515 (2015).
- [36] S. Duan, G. Tian, Z. Xie, and Y. Luo, *J. Chem. Phys.* **146**, 194106 (2017).
- [37] Z. Xie, S. Duan, C.-K. Wang, and Y. Luo, *J. Phys. Chem. C* **123**, 11081 (2019).
- [38] S. Duan, Z. Rinkevicius, G. Tian, and Y. Luo, *J. Am. Chem. Soc.* **141**, 13795 (2019).
- [39] S. Duan, G. Tian, and Y. Luo, *Angew. Chem. Int. Ed.* **55**, 1041 (2016).
- [40] Y. Zhang, B. Yang, A. Ghafoor, Y. Zhang, Y.-F. Zhang, R.-P. Wang, J.-L. Yang, Y. Luo, Z.-C. Dong, and J. G. Hou, *Natl. Sci. Rev.* **6**, 1169 (2019).
- [41] J. Lee, K. T. Crampton, N. Tallarida, and V. A. Apkarian, *Nature* **568**, 78 (2019).
- [42] Z. Xie, X.-R. Cao, L. Wang, H.-Z. Yu, C.-K. Wang, G. Tian, Y. Luo, and S. Duan, *J. Phys. Chem. Lett.* **14**, 363 (2023).
- [43] L. Yao, H.-Z. Yu, Z. Xie, and S. Duan, *J. Phys. Chem. Lett.* **15**, 10321 (2024).